ChemComm

ROYAL SOCIETY OF CHEMISTRY

REVIEW ARTICLE

View Article Online
View Journal

Check for updates

Cite this: DOI: 10.1039/d6cc02225a

Received 11th April 2026,
Accepted 3rd June 2026

DOI: 10.1039/d6cc02225a

rsc.li/chemcomm

Advances in iridium single-atom catalysts for the electrochemical oxygen evolution reaction

Dylan McFarlane-Urbszat, Raoul F. Vaz and Aicheng Chen *

Single-atom catalysts (SACs) have emerged as highly versatile catalytic materials for enhancing many industrially relevant electrochemical reactions. This review highlights recent advancements in the development of iridium SACs, primarily for water splitting applications. By reducing iridium to the single atom scale, the inherent beneficial scaling relationships can be preserved while substantially reducing precious metal loading to achieve mass activity as high as 2511 A g_{Ir}^{-1}. The single-atom character also allows for unique electronic and coordination interactions, resulting in oxidation states surpassing Ir(V) and enhancement of the lattice oxygen implementation, expanding the parameters for electrochemical performance optimization. Through this optimization, one highlighted catalyst was able to achieve an overpotential of 144 mV at 10 mA cm^{-2} for the oxygen evolution reaction, resulting in hydrogen generation surpassing the Department of Energy targets. Although currently limited by synthetic obstacles, the recent advances in Ir SACs highlighted in this review aim to show potential pathways towards commercial applications, contributing to the widespread implementation of zero emission hydrogen fuels.

Introduction

Despite being one of the scarcest elements on the earth, making up only 0.022 ppb of the earth's crust, iridium continuously proves essential in the field of electrocatalysis.[1,2] Iridium displays exceptional stability and activity for a number of electrochemical catalytic reactions, including fuel oxidation (*e.g.*, methanol and formic acid), the oxygen reduction reaction (ORR) and the oxygen evolution reaction (OER).[3–6] For the OER, in particular, the electronic structure of iridium places it near the peak of a linear scaling relationship resulting from thermodynamic similarities between hydroxide (HO*) and oxyhydroxide (HOO*) intermediates formed during the reaction, minimizing theoretically required overpotential.[7,8] Despite these advantages, a key direction of current electrocatalytic research is moving away from reliance on high loading iridium catalysts due to high cost and limited supply.[2,9] As a result,

Electrochemical Technology Centre, Department of Chemistry, University of Guelph, 50 Stone Rd E, Guelph, Ontario N1G 2W1, Canada. E-mail: aicheng@uoguelph.ca

Dylan McFarlane-Urbszat

Dylan Mcfarlane-Urbszat received his undergraduate degree from the University of Toronto and is now a PhD candidate at the University of Guelph with Prof. Aicheng Chen. His interests include the design and synthesis of heterogeneous iridium-based catalysts for the oxygen evolution reaction and sustainable energy applications.

Raoul F. Vaz

Raoul F. Vaz received his undergraduate and MSc degrees in Biophysics from the University of Guelph and is now a PhD candidate at the University of Guelph with Prof. Aicheng Chen. His interests include electrocatalyst development, additive manufacturing, and the design and fabrication of custom electrochemical cells for in situ characterization of electrochemical systems.

strategies that can reduce overall metal loading are attractive to reduce cost and supply chain risks at the industrial level while preserving the inherent advantages of iridium catalysts.

Substantial developments have been made in limiting iridium loading through the implementation of a number of techniques in parallel. Introduction of supporting materials to modulate the electronic structure allows for further enhancement beyond the previously described scaling relation.[10] Co-metal catalysts, such as IrTa,[6] IrRu,[11] and IrPt,[12] can enhance active sites through coordination site modification, while offsetting the loading requirements with less costly metals. Similarly, non-metal integration can reduce costs further by decreasing the metal loading altogether while still achieving beneficial modulation of the iridium active sites.[13] This is often achieved by decreasing the catalytically active metal to the nano-scale in the form of nanoparticles and nanostructures, with the non-metal playing the role of a support.[14] High surface area and conductivity supports, such as carbon-based structures, can increase dispersion and decrease charge transfer resistance, increasing performance despite a substantial decrease in active site density.[15] This concept is seen commonly in commercial products implemented in industrial water splitting, with iridium on carbon used frequently.[16] By combining nanoscale synthesis, co-metal catalysts and support engineering, the activity of iridium catalysts has been steadily improved.[17] Recent studies have looked into the implementation of activated carbon structures,[18] bulk phase engineering of nanoparticle activation,[19] and *in situ* nano structuring[20] to further minimize precious metal loadings and improve performance. Extrapolation of these concepts to their logical extremes would result in a catalyst that utilizes the minimum amount of iridium over a large and highly conductive surface with maximally tuneable active sites based on the coordination environment. The realization of this concept comes in the form of SACs. Since the report on their promising applications in electrocatalysis, the field of SACs has become an important avenue of study for numerous electrochemical reactions.[21] SACs serve to amplify the existing advantages of nanoscale precious metal catalysts while introducing new advantages not observed in nanoparticles.[22] In the water electrolysis reaction, iridium SACs have proved to be promising towards improving the oxygen evolution reaction (OER), which represents a major bottleneck. Through a number of strategies to be highlighted in this review, the overpotential of the OER is pushed below theoretical limits present in bulk materials with substantially reduced Ir loading. While some reviews have explored the topic of iridium SACs more broadly,[23] this review focuses exclusively on applications in water splitting, highlighting promising techniques and new strategies that can be applied for further development of iridium single atoms as efficient, high performance OER catalysts.

Aicheng Chen

Aicheng Chen is a Professor of Chemistry, Director of the Electrochemical Technology Centre at the University of Guelph, and a Tier 1 Canada Research Chair. His research spans electrochemistry, photoelectrochemistry, biosensors, and nanoscience. He has authored 320 peer-reviewed journal articles and nine book chapters. Dr Chen has received numerous honours, including the Ontario Premier's Research Excellence Award, a JSPS Invitation Fellowship, and major awards from the Electrochemical Society Canada Section and the Canadian Society for Chemistry. He is a Fellow of the Royal Society of Canada, the Chemical Institute of Canada, the Royal Society of Chemistry (UK), and the International Society of Electrochemistry.

Characterization

The primary and inherent advantage of SACs is the maximal atomic efficiency, with each individual atom acting as an available active site, allowing precious metal loading in the μg cm^{-2} scale to surpass mg cm^{-2} scale loadings on standard electrocatalysts.[24] Confirmation of maximal atomic efficiency is inextricably tied to the determination of whether a catalyst is truly "single-atom". For iridium catalysts, extended X-ray absorption fine structure (EXAFS) spectroscopy is often employed to confirm the single-atom character based on the absence of vicinal Ir–Ir contribution at the L_3 edge.[25] As illustrated in Fig. 1a, the absence of a peak at approximately 2.49 Å, when compared to Ir-foil, serves as the most widely accepted confirmation of atomic separation.[26] X-ray photoelectron spectroscopy (XPS) can also serve to characterize single-atom structure, and is often used in tandem with EXAFS for further structural confirmation.[27] Small shifts in binding energy can be detected, with Ir SACs often exhibiting binding energies slightly differing from IrO_2, IrCl and Ir-foil references due to changes in oxidation state, coordination or increased support interaction (Fig. 1b).[28] This alone is insufficient to confirm single-atom character, but can support other analysis to strengthen structural interpretations. Additionally, data from these sources can often be linked to specific structures through comparison with computationally modelled data generated using DFT calculations (Fig. 1c).

X-ray total scattering with subsequent pair distribution function (PDF) analysis, while only recently applied to SAC characterization, provides atomic pair correlations that determine structure through identification of nearest neighbouring atomic species.[29] This is achieved through application of the following PDF to an obtained scattering pattern (eqn (1)).[30]

$$G(r) = \frac{2}{\pi}\int_0^\infty Q[S(Q)-1]\sin(Q_\mathrm{r})\mathrm{d}Q \qquad (1)$$

where Q is the scattering vector determined by scatterer separation and $S(Q)$ is the structure function, normalization of scattering factors and the number of scatterers. Application of this function reveals short range structural correlations

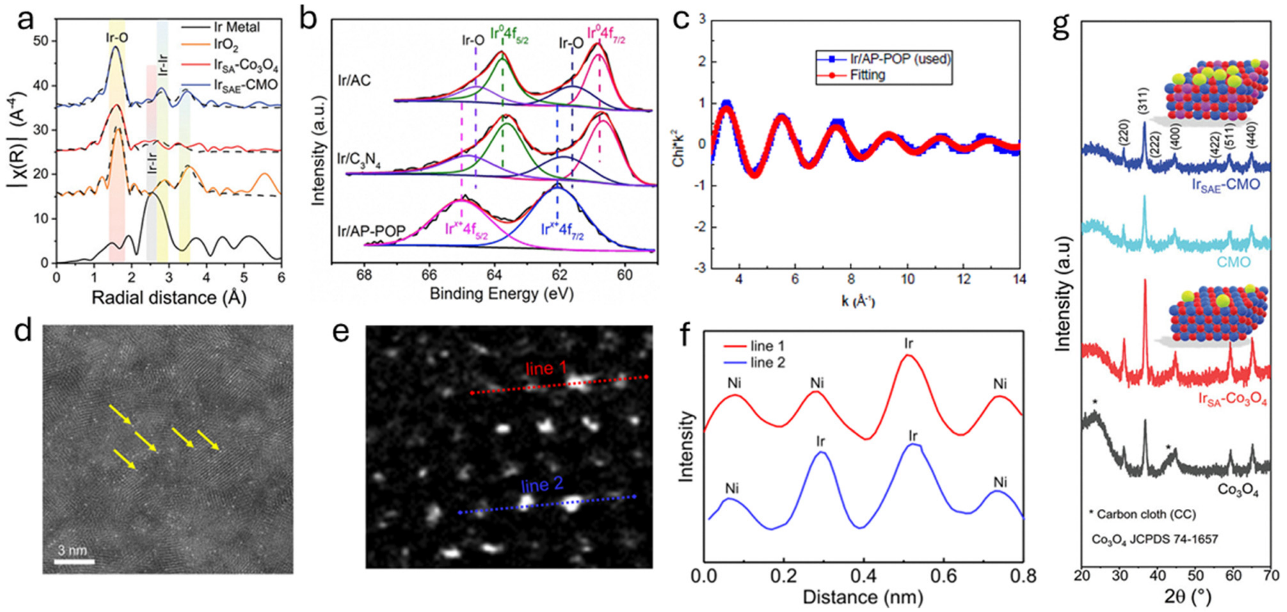

Fig. 1 (a) Comparative EXAFS of Ir Single atom and single-atom ensemble utilizing Ir metal and IrO_2 as standards. Reproduced with permission from ref. 27. Licensed under CC-BY-4.0. (b) XPS bonding environment of iridium SACs coordinated with different supporting materials demonstrating a shift in binding energy. (c) Fourier transform EXAFS data fitted with computationally generated spectra associated with structural calculations. Reproduced with permission from ref. 28. Copyright 2018 Elsevier Inc. (d–f) High resolution TEM and line intensity profile of iridium single atom catalysts showing an intensity difference between the iridium atom and the nickel background. Reproduced with permission from ref. 35. Licensed under CC-BY-4.0. (g) XRD comparison of single-atom iridium and support materials demonstrating peak broadening. Reproduced with permission from ref. 41. Licensed under CC-BY-4.0.

between atoms from the diffuse scattering intensity when compared to simulated structures. The presence of metal nearest neighbouring pairs serves as significant evidence that the existing catalysts are not uniformly single atom in nature, while the versatility and abundance of information extracted through this technique also allows for insights into the interplay between the support and active metal. Implementation of this technique *in situ* confirms the consistency of the single-atom structure, with any agglomeration of metal atoms resulting in the appearance of a new nearest neighbour contribution.[31] Application of PDF analysis allows for detailed structural recreations, substantially improving the accuracy of subsequent DFT analysis.[32]

Electron microscopy is also commonly used to confirm the presence of single atoms, with advanced techniques able to resolve individual SAC sites.[33,34] High-angle annular dark-field scanning transmission electron microscopy (HAADF-STEM) and high resolution transmission electron microscopy (HRTEM) are two common microscopy techniques used in SAC visualization due to the ability to directly visualize lattice structures (Fig. 1d–f).[35] These images can be analysed for electron intensity, allowing rough elemental characterization in the form of an intensity profile. While a useful tool, these profiles are limited in differentiating elements with similar atomic mass without the implementation of techniques to substantially enhance electron resolution to a sub-1 Å scale.[36] Energy dispersive X-ray spectroscopy (EDS), often used in tandem with electron visualization in the form of mapping, allows for elemental identification of the components of a single-atom catalyst. While most modern EDS instruments allow sufficient resolution to confirm the presence of the catalytic material of an SAC, highly specialized instrumentation can achieve atomic resolution EDS mapping, allowing for further confirmation of single-atom character.[37]

The methods outlined previously, while providing the gold standard for atomic structure characterization, often require access to synchrotron radiation or a free electron laser for high quality data in the case of EXAFS and PDF analyses, or highly specialized electron microscopy instrumentation in the case of HAADF-STEM.[38,39] Initial and large batch characterization can often be performed using sample specific methods on more accessible instruments. XRD is commonly employed in this role by comparing crystal structures of the support with and without the addition of SACs.[40] The addition of SACs can often result in disruptions in the crystal plane, resulting in peak broadening while simultaneously revealing that crystalline iridium structures have not formed through the absence of standard iridium peaks (Fig. 1g).[41] These results are dependent on the structure of the catalyst, as deposited single atoms on the surface of an existing lattice are unlikely to visibly affect the XRD pattern unless the deposition results in significant alteration of the lattice structure. Raman spectra can also be used for this purpose, with substitution of metals into a lattice resulting in a notable red shift in Raman active compounds. By identifying the band with the most pronounced shift, structural information such as preferred substitution location can also be determined.[42]

Synthesis and OER activity

Synthesis of SACs is highly variable, with methods using the same materials resulting in distinct structures and electrochemical performance.[43] These methods can be broadly divided into two major categories based on the resultant structure: superficial and lattice implemented. Generally, superficial synthesis methods result in a catalyst structure consisting of single atoms out of plane from the overall lattice, such as surface adsorbed single atoms, while lattice implemented catalysts incorporate active sites in the plane of an existing lattice, such as through vacancy engineering (Fig. 2a).[44,45] L_3 edge EXAFS of CoOOH catalysts with either lattice implemented or superficial Ir single-atoms demonstrates an important difference between the two structures. The catalyst with superficial Ir single-atoms shows increased Ir–O bond length for the superficial catalyst, indicating an unsaturated coordination environment (Fig. 2b and c).[44] This allows much of the aforementioned coordination tunability of superficial SACs, permitting even *in situ* modification through application of external fields.[46] A primary drawback of superficial SACs is likewise connected to the unsaturated coordination environment, with aggregation of surface particles into single-atom ensembles and nanoclusters often thermodynamically favorable.[47] For this reason, increasing loadings while maintaining atomic dispersion is a major challenge at the synthetic stage.[48,49] By substituting an existing element of the lattice structure with a single atom, lattice implemented SACs have a more complete coordination environment, though tunability is limited when compared to superficial SACs. By compromising on this benefit, single atoms are more tightly anchored within the lattice, which reduces the effects of aggregation and increases synergistic effects from neighbouring atoms.[50] While generally more stable, lattice implemented SACs may also suffer from restructuring during use under harsh acidic conditions, common for enhancing various electrochemical reactions.[51] This may result in the formation of surface nanoclusters, causing stability to be a major consideration in SAC design.[52]

Superficial iridium SACs

In situ cryogenic photochemical reduction of iridium on NiFe

One approach to prevent surface agglomeration involves the implementation of cryogenic freezing with *in situ* photochemical reduction.[53] The implementation of flash freezing with liquid nitrogen during the addition of the iridium precursor solution ensures that homogeneous distribution is maintained during the deposition process. The resulting ice can then be directly exposed to UV light under low temperature conditions, reducing the iridium precursor and depositing a well-distributed layer of iridium single atoms onto the Ni_9FeOOH support as illustrated in Fig. 3a. While cryogenic UV photoreduction has been applied previously as an individual step in a complex MOF based single atom synthesis, the method presented allows surface deposition, making the process theoretically applicable to a number of metal/support combinations.[54] The HAADF-STEM image and the Ir-L_3 edge EXAFS spectra confirmed the single-atom character of the deposited iridium (Fig. 3b–d), revealing no distinct peaks in the Ir–Ir bond location when compared with an iridium foil. Using the established XANES white lines method, an oxidation state analogous to the Ir^{4+} state was identified at open circuit voltage (OCV). A series of *in situ* XANES measurements reveal a peak with an average oxidation state of $Ir^{5.3+}$ at the applied electrochemical potential of 1.45 V *vs.* RHE, with the major oxidation from the Ir^{4+} analogous state occurring before 1.35 V *vs.* RHE and a decrease of the average state occurring at 1.55 V *vs.* RHE. These findings were consistent with DFT and observational core-level excitations with *ab initio* nitrogen-based technique (OCEAN) calculations, which implement photon polarization and momentum dependence in computing XAS spectra.[55]

As shown in Fig. 3e, the resulting catalyst exhibited remarkable OER performance and stability despite the relative simplicity of the synthetic method. An OER overpotential of 183 mV at 10 mA cm^{-2} was achieved, surpassing the 280 mV benchmark characteristic of the high end commercial IrO_2 catalysts. The high OER activity was attributed to the decrease of available 5d electron density for binding with 2p oxygen states, thus

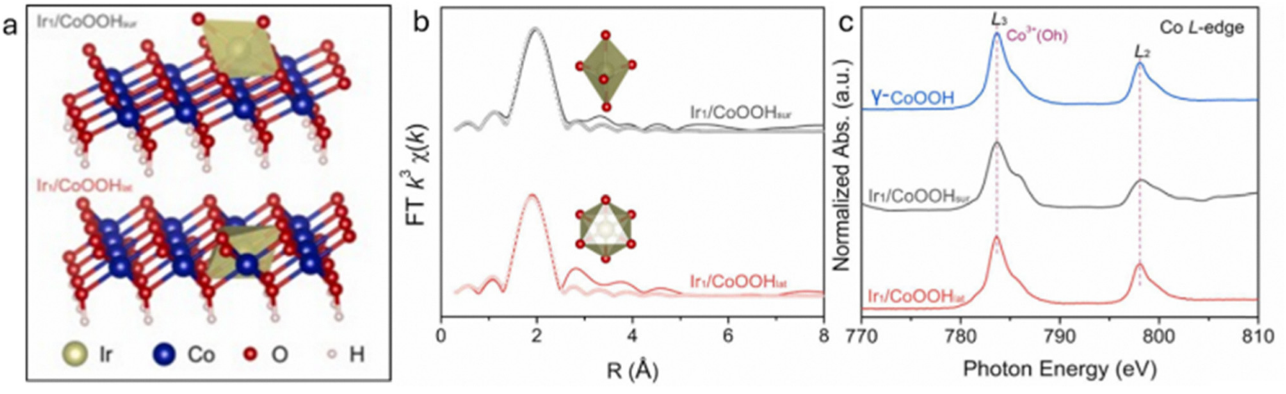

Fig. 2 (a) Visual depiction of the structural difference in lattice implemented and superficial SACs. (b and c) Ir and Co L_3-edge EXAFS spectra comparing surface adsorbed and lattice implemented SACs. Reproduced with permission from ref. 44. Copyright 2023 Elsevier B.V.

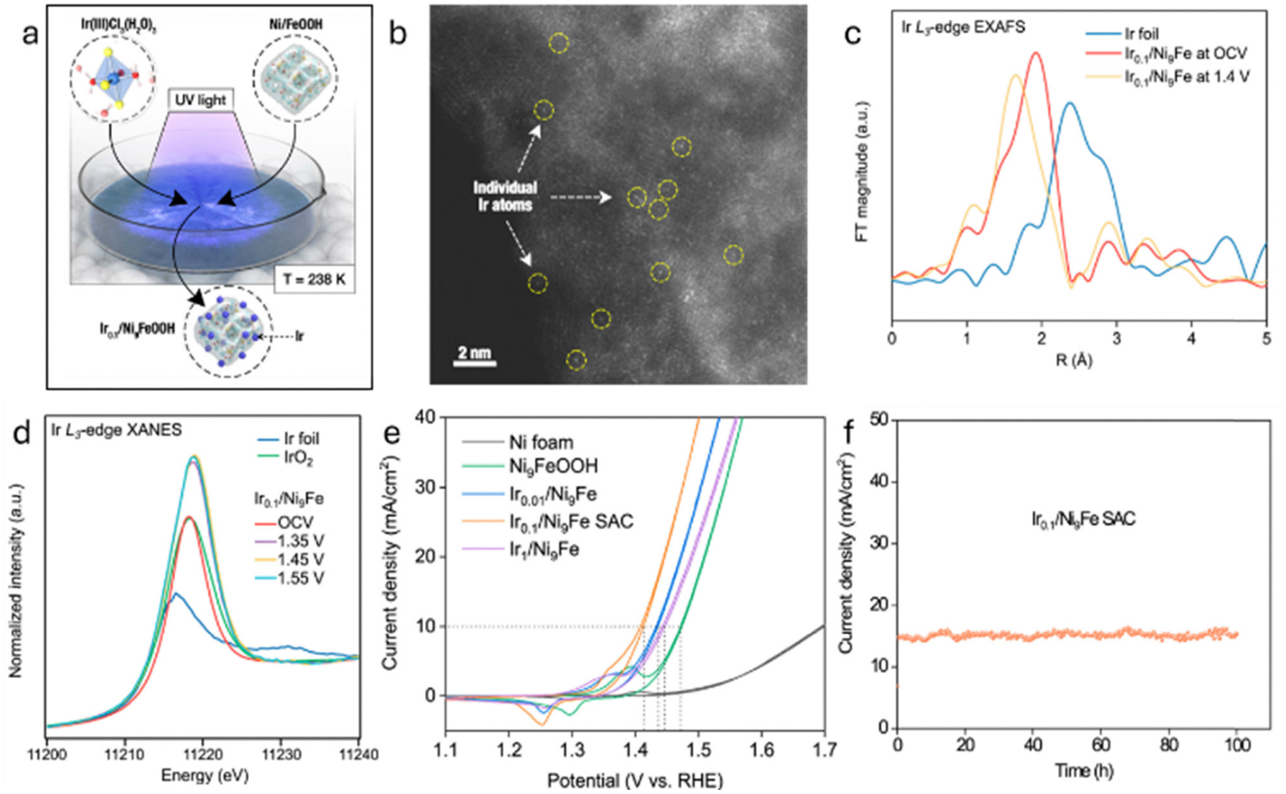

Fig. 3 (a) Graphical depiction of *in situ* UV reduction coupled with cryogenic freezing. (b) HAADF-STEM image of the resulting single-atom catalyst. (c) Ir L_3-edge EXAFS at OCV and 1.4 V with an Ir-foil reference. (d) Ir L_3-edge XANES showing a WL shift in-site against Ir foil and IrO$_2$ references. (e) LSV sweep to 1.7 V of various iridium loadings in SAC synthesis compared to nickel foam and unmodified nickel iron. (f) Chronopotentiometric stability of the high-performance catalyst at 1.43 V *versus* RHE for 100 h. Reproduced from ref. 53. Licensed under CC-BY-4.0.

reducing adsorbate bonding strength and optimizing energetic barriers to improve the potential limiting step. This electronic environment was found to be highly dependent on loading mass, with optimization determining that ∼1% iridium content achieved minimal overpotential. Exceptional stability was also demonstrated at an overpotential of 200 mV over 100 h, showing no appreciable loss in current density (Fig. 3f). This method demonstrates high performance while minimizing the effect of agglomeration, showing great promise. Additional work looking at performance and stability at potentials more common in industrial settings (∼2 A cm^{-2} for AWE) as well as the feasibility of application on other common supports could encourage widespread adoption of this synthetic technique.

Structural modification of iridium coated Ni nanospheres

As agglomeration often occurs during the reduction from the dissolved ion in solution to the solid metal state, one method to bypass this limitation involves nano-structuring during this initial step and then separating the individual atoms. This approach is exemplified using chemical modification of iridium shelled nanoparticles to achieve atomization.[56] This method takes advantage of the core–shell structure generated by iridium and nickel at the nanoscale. By continuously introducing phosphate in a high temperature environment, a Kirkendall void is generated at the center of the nickel nanosphere, resulting from the nonreciprocal interdiffusion at the Ir/Ni interface.[57] The expansion in surface area resulting from the introduced hollow volume of the Kirkendall void causes uniform atomic disruption of the iridium shell (Fig. 4a–d). Comparison between simulated and experimental HAADF-STEM images revealed that the Ir SACs reside selectively on the surface of the lattice, allowing accessibility to all iridium active sites. XANES spectra of the Ni-K edge demonstrated a decreased oxidation state due to the presence of iridium in the coordination environment, while the L_3-Ir edge showed a similar oxidation state to IrO$_2$, attributed to formation of Ir–O–P (Fig. 4e and f). The fitted EXAFS data help to complete the picture of the atomic scale bonding, with Ir–O–P and Ni–O–P dominating the process (Fig. 4g).

Analysis of OER activity showed an overpotential of 149 mV at 10 mA cm^{-2}, outperforming commercial IrO$_2$ as well as NiP nanospheres. Additionally, the catalyst was able to achieve a current density of 154 mA cm^{-2} at an overpotential of 300 mV, showing a larger working range, yet still well below potentials required in a commercial AWE (Fig. 4h). Stability was tested at 1.5 V *vs.* RHE for 40 h, with a 2.1% decrease in current density (Fig. 4i). These metrics were further explored with DFT calculations, showing that Ir doping significantly promoted chemisorption of OER intermediates to the NiP surface. Quantitatively, the bonding contribution from Ni–*O to Ir–*O changed by −0.74 eV, as shown using integrated crystal orbital Hamilton population (ICOHP) (Fig. 4j). Despite the detailed understanding of structure and mechanism, no analysis was

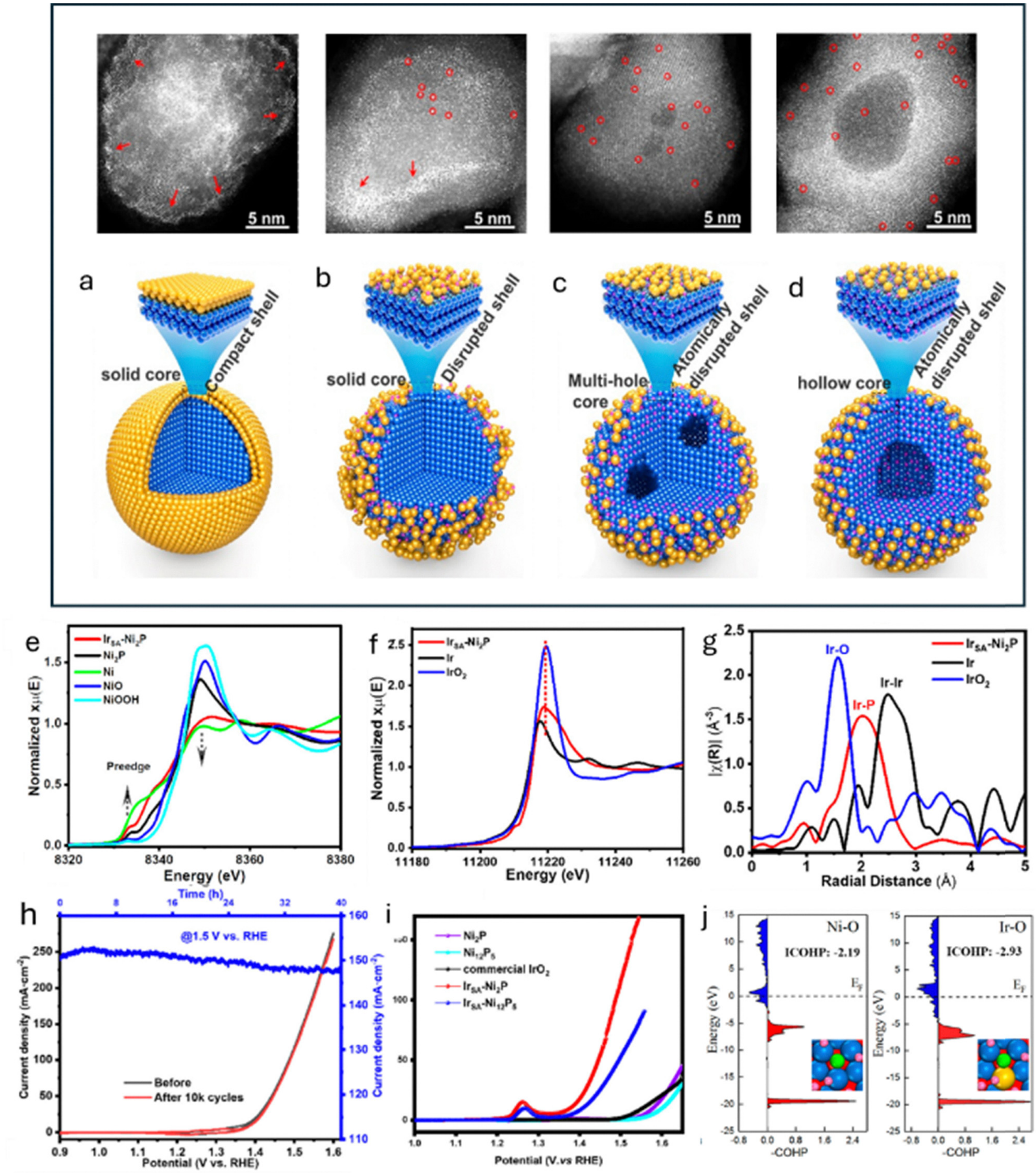

Fig. 4 (a–d) HAADF images and renders at differing temperatures to simulate the expansion of nanoparticles used to isolate the iridium shell. (e) Ni K-edge XANES showing a decreased oxidation state in the presence of iridium SACs. (f and g) Ir L_3-edge XANES and EXAFS demonstrate the isolated bonding environment with IrO_2 and Ir foil references. (h) LSV sweep to 1.6 *vs.* RHE of different catalysts including and excluding iridium single atoms. (i) LSV and CA demonstrating stability. (j) Calculated bonding orbitals for Ni–O and Ir–O using the ICOHP method. Reproduced with permission from ref. 56. Copyright 2021 American Chemical Society.

performed under industrially simulated conditions or with regard to scaling of the method, indicating a technology still in its infancy.

Direct writing on polyimide support

Conventional electrode fabrication typically involves coating catalyst inks onto 2D planar substrates, which often suffers from uncontrolled catalyst distribution, binder blockage of active sites, and poor mass transport of reactants and gaseous products at high current densities.[58] To address these limitations, additive manufacturing (3D printing) has emerged as a transformative technology for the scale-up of SACs, enabling the direct construction of hierarchically porous, macroscopic electrodes with precise control over geometry and active site distribution.[59]

A primary concern for the application of additive manufacturing lies in compatibility between the manufacturing and synthetic techniques. Due to this, materials compatible with existing and well-distributed methods of additive manufacturing are receiving notable interest. Providing a blueprint for such materials, an atomically dispersed Ir catalyst supported on polyimide (PI) was recently reported, which exhibits exceptional stability in acidic OER using a fabrication technique that can be directly translated into Direct Ink Writing (DIW) and stereolithography, where PI precursors are standard feedstock materials (Fig. 5a).[60] HAADF-STEM measurements (Fig. 5b) demonstrate the single-atom nature of these catalysts, with DFT calculations (Fig. 5c) revealing the effect of electron-rich and deficient moieties on the electronic structure of the metal centers. XAS measurements (Fig. 5d and e) demonstrate similarities in the structure and coordination environment between IrO_2 and single-atom iridium centers in the synthesized material. The resulting catalyst (Ir–PI@CP) demonstrated superior performance (Fig. 5f–i) and negligible activity decay over 360 h of operation in 0.5 M H_2SO_4, a stability attributed to the strong electronic coupling between the iridium 5d states and the electron-rich amine/electron-deficient anhydride moieties of the polymer backbone. Stability was confirmed with FTIR, XRD and XPS measurements, showing no obvious structural changes, and through a decrease in iridium dissolution over time.

Theoretical calculations revealed that this specific coordination environment lowers the energy barrier for the formation of the *OOH intermediate, the rate-determining step in the OER mechanism. For the field of 3D printing, this work, alongside other recent developments, further establishes PI not just as a structural plastic but as a functional electrochemical support.[61] An incidental advantage of a PI substrate is its compatibility with *in situ* and *operando* investigations into catalytic activity using synchrotron radiation (XAS, XRD, and PDF analysis), as it is a commonly used window material for electrochemical cells.[62] While *ex situ* analysis using these methods has become increasingly routine, *in situ* and *operando* electrocatalyst characterization is essential to understand the nature of SAC performance. Thus, PI is an extremely attractive material (commonly known as Kapton®) that can be utilized through the entire development cycle of a SAC from lab-based synthesis and characterization to mass production, where it is simultaneously the carbon source for graphene-based SACs and the conductive electrode ''support'' for the catalyst, which simplifies synthesis. Future efforts could focus on extruding Ir-doped polyamic acid inks to create 3D-printed lattices that are subsequently

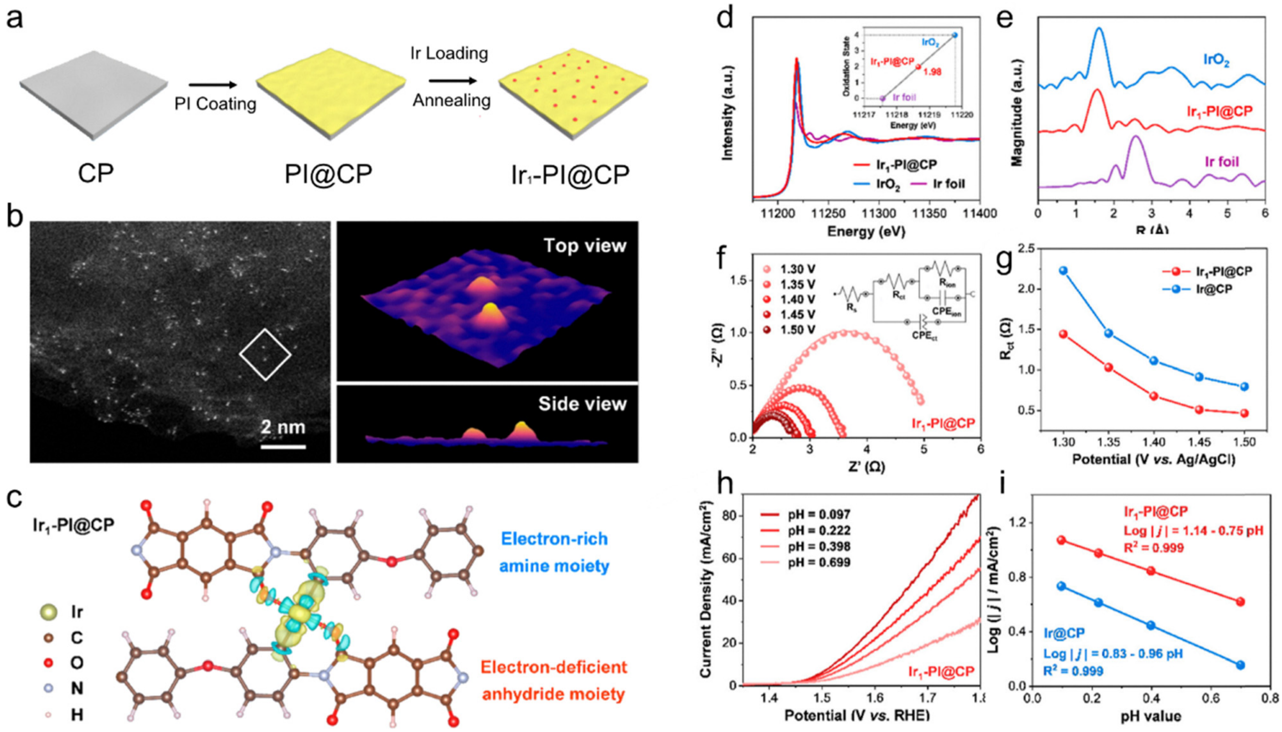

Fig. 5 (a) Iridium SACs on a polyimide (PI) substrate in a simple 2 step process. Supported by (b) HAADF-STEM measurements, (c) DFT calculations, (d and e) XAS measurements, the single-atom nature of the catalyst, and local electronic environment around the iridium metal centre enhances the catalytic activity for the OER. (f–i) Electrochemical characterization demonstrate the superior performance of the SAC when compared to metallic iridium. Reproduced with permission from ref. 60. Copyright American Chemical Society.

imidized, combining the macroscopic mass-transport benefits of 3D printing with the atomic-scale stability of the Ir-PI coordination.[63]

Lattice implemented iridium SACs

Templating of iridium single atoms on cobalt spinel structures

Substitution of single atoms into an existing lattice is a commonly employed technique for the synthesis of lattice implemented SACs. This is illustrated in Fig. 6, where SAC synthesis was achieved through substitution into an existing template lattice structure, a Co-based zeolitic imidazole metal–organic framework (MOF), resulting in a single-atom iridium doped cobalt spinel structure.[42] By substituting iridium into the existing Co cationic sites, identical spatial correlation is preserved, altering the favourable coordination environment as compared to iridium nanostructures (Fig. 6a). This results in formation of short-range ordered iridium clusters of 1–13 atoms, composed of a single-atom and cluster hybrid system with the mass fraction of sites of a specific number of atoms decaying exponentially with increasing number of atoms. This structure was confirmed by atomic resolution HAADF–HRSTEM, showing primarily individual iridium structures through PDF calculations and revealing deposition within the octahedral sites of the cobalt spinel structure (Fig. 6b and c). XANES spectra of the Ir L_3-edge supported valence state assignment of approximately +4, while EXAFS spectra showed major peaks at interatomic distances assigned to Ir–O and Ir–Co_{oct}. Unlike strictly single-atom structures, there is a minor contribution from a peak assigned to Ir–Ir (Fig. 6d and e). Electrocatalytic OER performance evaluation showed a current density of 5.99 mA cm^{-2} at an overpotential of 300 mV. Combined with the low iridium loading mass, this results in an exceptional mass activity of 2511 A g_{Ir}^{-1} (Fig. 6f). Stability tests showed an increase in overpotential of 84 mV at 10 mA cm^{-2} over 200 h (Fig. 6g). The stability is attributed to the suspension of the Co(III)/Co(IV) redox pair resulting from Ir substitution. This was further supported through DFT calculations, demonstrating a down shifted valence band maximum edge of Co_{oct}, resulting in a decreased tendency to oxidize. These calculations also demonstrated a localized Ir 5d–O 2p state near the Fermi level, contributing to increased charge transfer. Despite lower performance metrics, this catalyst demonstrates an important technique in the development of Ir SACs.

Multi-step atomic assembly of single-atom iridium in ruthenium nanoclusters

Another approach to lattice implemented SAC synthesis was demonstrated in a recent study, combining a series of chemical steps to atomically assemble the overall catalyst.[64] These sequential steps include hydrothermal growth of Na–titanate, cation exchange between Na and Ru^{3+}, calcination of Ru–titanate and galvanic replacement of single Ru sites with Ir. The resulting structure consists of hexagonal Ru nanoparticles with lattice implemented iridium single atoms, embedded in a TiO_2 support (Fig. 7a). This structure was confirmed by atomic resolution STEM, where both the Ru nanoparticles and iridium single atoms were identified based on differing intensities (Fig. 7b–f). EXAFS of the Ir L_3-edge showed a main peak corresponding to a band length of 2.40 Å, falling between Ir–Ir at 2.49 Å and Ir–O at

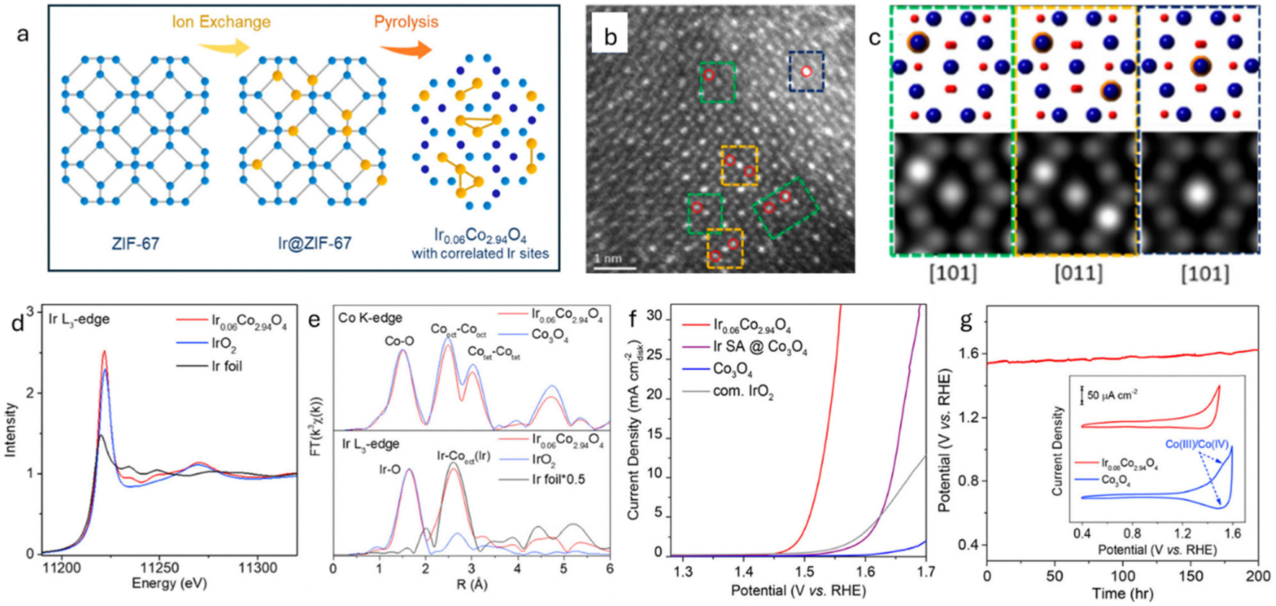

Fig. 6 (a) Scheme displaying the two-step template-based synthesis process. (b and c) Resultant atomic structures pictured through HR-TEM compared to simulated structures. (d) Ir L_3-edge XANES and EXAFS as well as Co K-edge EXAFS give a detailed picture of the oxidation state and coordination environment. (f) OER performance compared between different iridium derivations of Co_3O_4 and commercial IrO_2. (g) Chronopotentiometric determination of catalytic stability with the inlet displaying supressed Co(III)/Co(IV) redox with iridium addition. Reproduced with permission from ref. 42. Copyright © 2021 American Chemical Society.

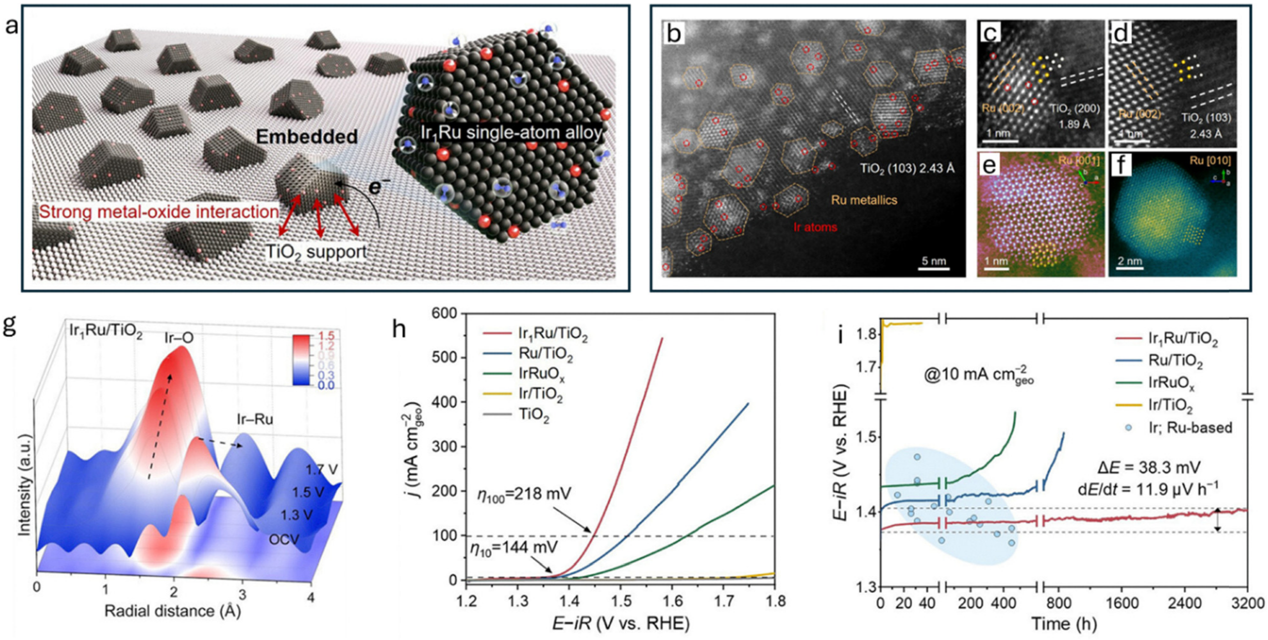

Fig. 7 (a) Graphical depiction of Ir SACs implemented within Ru nanoclusters on a TiO_2 support. (b–f) Atomic resolution STEM images confirming a simulated structure. (g) *In situ* Ir L_3-edge EXAFS spectra demonstrating changes in structure with applied potential. (h) Electrochemical OER performance compared to relevant similar catalysts. (i) Long-term chronopotentiometric determination of stability. Reproduced with permission from ref. 64. Copyright 2025 Wiley-VCH GmbH.

1.59 Å, which was attributed to Ir–Ru (Fig. 7g). DFT calculations associated with this structure demonstrated enhanced electron density at metal centers resulting from TiO_2 support, further stabilization of Ru active centers by iridium and a downward shift in d-band centers resulting in weaker bonding of OER intermediates.

The resulting catalyst was tested for OER activity in 0.5 M H_2SO_4, showing overpotentials of 144 mV and 218 mV at 10 mA cm^{-2} and 100 mA cm^{-2}, respectively (Fig. 7h). These metrics not only outperform most acidic OER catalysts but even outperform the more facile alkaline OER in many cases. The overpotential at 10 mA cm^{-2} underwent a 38.3 mV increase after 3600 h, showing the high stability characteristic of lattice implemented SACs (Fig. 7i). Further investigation into electrochemical efficiency revealed the decrease of charge transfer resistance and facile surface deprotonation, resulting in an overall decreased activation energy for the OER. Coupled computational DFT calculations and experimental surface enhanced infrared absorption spectroscopy (SEIRAS) spectra indicated that the addition of Ir SACs prioritized the AEM pathway while stabilizing the HOO* intermediate, effectively balancing the OER linear scaling relation. Iridium also stabilized higher Ru oxidation states while supressing the readily dissolved Ru^{4+} and Ru^{6+}. Additional testing was performed using a lab-scale PEMWE with the catalyst acting as both an anode and a cathode. Achieving cell voltages of 1.611, 1.712, and 1.785 V at 1.0, 2.0 and 3.0 A cm^{-2}, respectively, places this technology above the DOE PEMWE targets for 2026 and only slightly below the ultimate targets set by the agency.[65] The cell voltage also remained below targets after 2000 h of continuous use at 3 A cm^{-2}. This catalyst demonstrates a significant step forward in the development of and understanding the potential of Ir SACs; however, the complex synthesis of the catalyst limits its ability to scale up to industrial quantities.

Universal scalable conversion of bulk metals into single atoms

Industry scale automation of chemical processes can often be complex and favor existing mature technologies that are widely understood. Electrodeposition then serves as a primary candidate, tracing its scientific origins back over 250 years.[66] Since then, electrodeposition has been widely applied in industry as a method of low material use, highly precise manufacturing applied in industries ranging from iron and steel production to microchip fabrication, as well as serving as an essential technology in catalyst development.[67] Due to the extensive automation work performed in these industries, a one-step electrodeposition synthesis technique for Ir SACs could be straightforwardly scaled up to industrial quantities.

A recent study outlines a universal method of transformation of bulk metals into SACs through the use of precisely controlled electrodeposition.[68] This method was demonstrated to be effective for twenty different monometallic SACs, including Ir SACs. The formation of SACs was achieved through co-optimization of a series of variables, primarily focusing on potential and viscosity, given a large working range through the use of a chlorinated deep eutectic solvent (DES), while taking advantage of electrostatic barriers to agglomeration in high ionic strength solutions. Electrodeposition was performed using cyclic voltammetry where the chlorine ions in the solvent form chlorinated complex ions with the bulk metal before moving through solution to the cathodic surface and

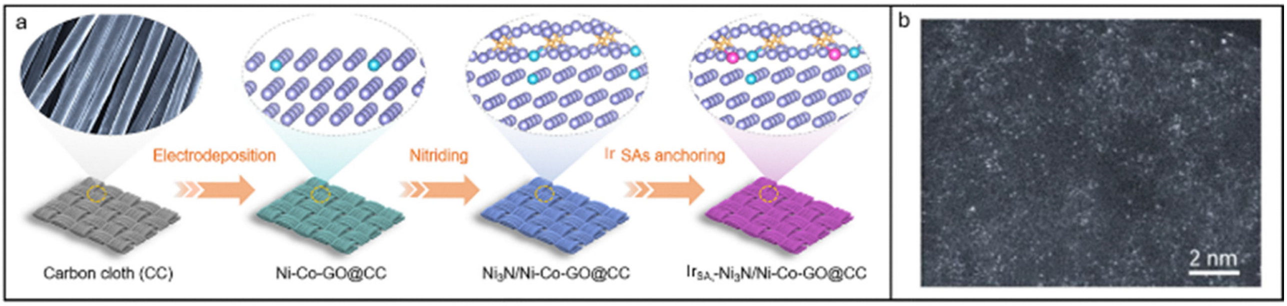

Fig. 8 (a) Graphical depiction of Ir SAC electrodeposition on carbon cloth. (b) Atomic scale HAADF-STEM image of Ir SACs. Adapted with permission from ref. 68. Licensed under CC-BY-4.0.

depositing on engineered vacancies in the support material, forming the SACs (Fig. 8a). The overall mass loading of the SACs can be controlled based on regulation of CV cycling.

While extensive testing for the validation was only performed on Pt SACs, some fundamental characterization was performed on alternative metal SACs including iridium. XPS analysis was performed focusing on the iridium 4f peak, with high resolution fitting indicating a valence state shifted slightly from IrO_2 and Ir-foil, associated with single-atom binding sites. In addition, the XRD patterns demonstrate a slight alteration in the crystal structure of nitrogen doped graphene expected from the formation of the surface interface layer, with no peaks associated with iridium metal present, indicating that no iridium cluster crystal structures have formed. The HAADF-STEM atomic scale image (Fig. 8b) demonstrates the surface structure while further confirming single-atom nature alongside EDS displaying the distribution of the single-atom structures across the catalyst surface. OER testing has not been performed on catalyst fabricated using this technique as the initial validation focused on cathodic reactions such as the HER; however, due to the variability of loadings and support materials, additional work focused on optimization of an OER catalyst using this method would be valuable.

Theoretical calculations and mechanistic studies

Iridium SACs have emerged as a promising next generation of catalytic materials, combatting the increasing economic disadvantages of precious metal catalysts while benefiting from the numerous advantages, further enhanced by the single-atom structure. As demonstrated throughout this review, the oxygen evolution reaction is a major beneficiary of this emerging technology. Due to the breadth of combinations of structures and supports available for Ir SACs alongside the extensive versatility, there are many beneficial effects that can explain the demonstrated enhancement of electrochemical performance. The most common and well understood of these include an increased stable oxidation state, access to more efficient reaction pathways and increased tunability, allowing energy optimization beyond the limit of traditional nano-catalysts. As discussed previously, the linear scaling relationship between OER intermediates serves as a limitation for conventional OER optimization. These unique attributes of SACs can result in subversion of this linear scaling relation in a number of ways in order to approach ideal OER kinetics.[69]

The first of these attributes is the stabilization of non-preferred oxidation states. By using XANES spectra to determine oxidation states based on white line position, iridium SACs have shown *in situ* oxidation states above Ir^{5+}, not commonly seen in standard iridium materials or nanoparticles (Fig. 9a and b).[70,71] This serves to increase the adsorption strength of precursors in several electrochemical reactions, with DFT calculations demonstrating a particularly strong correlation between the oxidation state and OER performance in iridium double perovskites, with Ir^{6+}, the highest oxidation state, resulting in the best electrochemical performance.[72] While this work is not inherently generalizable to all Ir SACs, the trend is observed within this review with many highlighted catalysts attributing enhanced performance to the increased oxidation states.

The high tunability of SACs also contributes to increased electrochemical performance, with a much wider range of optimizations possible compared to nanostructured metals.[73] DFT calculations show OER energetic barriers on a number of possible iridium SAC configurations on a covalent organic framework (Fig. 9c and d).[74] By selectively modifying the valence state of the Ir SACs through slight configurational alterations, the energy required for each OER step can be optimized to near identical levels, substantially reducing the predicted overpotential. This was achieved through optimization of a number of factors to create an oxidative microenvironment that could maximize the oxidation state and enhance the formation of an OIrOH active-site. The high susceptibility of SACs, especially superficial SACs, to external conditions allowed for minute changes to substantially affect performance, resulting in a much wider range of possibilities for optimization. These calculations revealed predicted overpotentials as low as 0.23 V, surpassing the limitation imposed by the scaling relationship.

The introduction of SACs can also influence reaction mechanisms, resulting in more favourable pathways being enhanced.[75] The classical OER mechanism uses oxygen

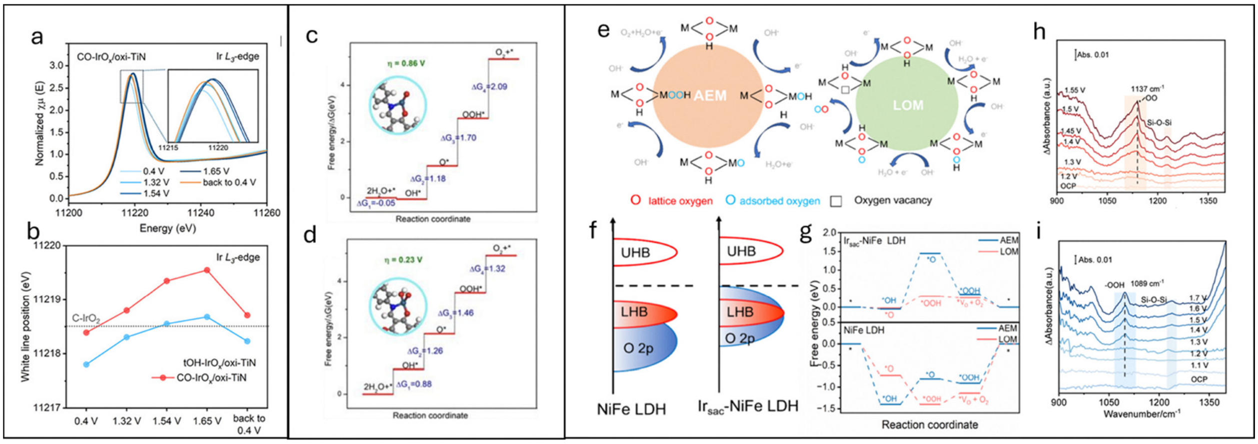

Fig. 9 (a and b) Ir L_3-edge XANES demonstrating a WL shift with potential and a plotted white line potential comparing the WL shift of different catalysts with that of IrO_2. Reproduced with permission from ref. 71. Copyright 2025 Wiley-VCH GmbH. (c and d) Free energy diagrams demonstrating the tunability of Ir-SACs with non-ideal (c) and ideal (d) OER scaling, resulting from small configurational changes. Reproduced with permission from ref. 74. Copyright 2025 American Chemical Society. (e–g) The adsorbed and lattice oxygen mechanisms of the OER are depicted with band gap and DFT calculations, demonstrating the advantages of the lattice oxygen mechanism. (h and i) ATR-SEIRAS of a NiFe catalyst with (h) and without (i) iridium SACs, demonstrating a mechanistic shift. Reproduced with permission from ref. 78. Copyright 2025 Wiley-VCH GmbH.

adsorbed onto a catalytic surface. There has been a recent investigation into an alternative mechanism that implements lattice oxygen instead.[76] While this behaviour has been demonstrated in meticulously engineered bulk materials and has shown high activity, it also results in structural degradation of the catalytic material under harsh OER conditions.[77] Enhancement of this lattice oxygen mechanism (LOM) using Ir-SACs on NiFe was recently demonstrated, effectively subverting limitations intrinsic to the standard OER linear scaling relation while also bypassing the structural limitations seen in the bulk equivalents (Fig. 9e).[78] Projected density of states calculations show that the introduction of iridium SACs results in an upward shift in the O 2p band center, increasing the overlap of the lower Hubbard band and enhancing electron flow upon application of current (Fig. 9f and g). This increased hybridization facilitates the implementation of lattice oxygen, resulting in lowered activation energy for the LOM of the OER. This enhancement allows the LOM pathway to dominate the standard adsorbate evolution mechanism (AEM). *In situ* attenuated total reflection surface-enhanced infrared absorption spectra (ATR-SEIRAS) of the NiFe catalyst with (Fig. 9h) and without (Fig. 9i) iridium SACs confirm the shift in mechanism. The iridium SAC containing catalyst shows a significant peak at 1136 cm^{-1} increasing with potential, attributed to rapid accumulation of the O–O radical intermediates seen in the LOM pathway. For the non-SAC catalyst, a peak is seen at 1089 cm^{-1}, attributed to the production of the integral *OOH intermediate of the AEM mechanism. The single-atom LOM catalyst subverts the expected decrease in stability with 1000 h of OER operation showing negligible loss in performance. Due to the multiple methods of enhancement available through SACs, considerable tuning can be performed for various electrochemical reactions, with the OER only serving as one particularly relevant example.[44]

Research gaps and future work

One notable limitation of the majority of nearly all the highlighted studies discussed in this review is the high specificity of the synthetic methods to the applied materials. Expansion of these techniques to alternative supporting materials and co-active sites would allow for identification of useful trends and assist in rational catalyst design. As an example, the *in situ* photochemical reduction technique used for $Ir_{0.1}/Ni_9Fe$ SACs can be theoretically applied to a number of supports with comparable or tuneable band gaps to accommodate the photoreduction of iridium, representing a possible avenue for future research. In addition, a lack of specific studies related to stability within the field serves as another barrier to rational catalyst design. While stability metrics are cited for each of the highlighted papers, the lack of standardization and the wide range of times and conditions make the analysis of stability trends impossible to discern. Specific analysis of stability, in particular dissolution pathways, has been conducted for bulk and nanoscale iridium and iridium oxide, allowing for intentional steps to be taken to improve stability; however, any differences in the presented single atoms are notably understudied and are essential in moving the field towards commercialization.[80]

The most critical gap present in the development of iridium SACs remains between laboratory-scale powders and industrial-scale Ir SAC electrodes, with the limited existing scalable techniques unable to capture the breadth of advantages possible in academic settings.[81] The lack of scalable techniques for fabrication of Ir SACs can be reinforced by integrating the promising techniques currently developed for other transition metal based SACs. Application of these strategies to Ir SACs would result in a substantial increase in fabrication capabilities. A persistent challenge in the use of structured supports—whether 3D printed or conventional—is the adhesion of the catalytic layer, particularly in highly stressful environments such as industrial Membrane

Electrode Assemblies (MEAs).[82] Under the conditions of high current densities and shear-stress, the latter due to both the electrolyte flow rate and gas-evolving reactions, wash-coating or impregnation methods often result in catalytic coatings that are prone to delamination, which may not manifest under often idealized laboratory conditions in which they are developed.[83] To overcome this mechanical failure mode, a recent study pioneered a fabrication strategy using high-resolution digital light processing (DLP) in the form of a photopolymer based resin 3D printer.[84] Producing complex geometries which maximize available surface area and optimize flow can prove to be difficult, if not impossible, with traditional manufacturing techniques, and the feasibility of utilizing advanced techniques like multi-axis CNC milling becomes questionable if the intent is mass production.[85] However, these complex geometries such as triply periodic minimal surfaces (TPMSs) are supported by all consumer-grade 3D printers, and are used extensively as a means of saving material, and reducing manufacturing time. Instead of simply coating a 3D-printed or conductive substrate with catalytic material, the SAC was directly integrated into the photopolymer resin during the curing process, producing a single monolith. Using a nickel SAC on carbon nitride (C_3N_4) as a model system, complex spiral-twisted static mixers that functioned as both catalytic beds and flow reactors were successfully printed. A catalyst to resin mass ratio of 1 : 100 was found to be optimal, as a higher catalyst content resulted in structural defects due to scattering of UV irradiation utilized for curing, while a lower content reduced the performance of the reactor. This methodology is particularly promising for iridium SACs, as it suggests that Ir-based SACs on a carbon-based support could be similarly dispersed into UV-curable resins to produce standalone electrodes, where active sites are embedded throughout the matrix, rather than just on the surface of a conductive substrate. While the accessibility of the catalytic material in the bulk of the printed monolith to reactants is a concern, integration of the catalytic material directly into the support confers significant advantages to mechanical stability, maximum surface area, and maintaining optimized flow geometries. This is a particularly promising application of additive manufacturing with Ir-SACs in the OER, as it has been demonstrated that the utilization of TPMS electrode geometries under forced electrolyte flow provides significant performance enhancements.[86]

Beyond structural support and mass transport optimization, the transition into 3D macroscopic architectures enables the integration of auxiliary functions directly into the catalyst body. This was recently demonstrated, with engineering of a copper SAC into a self-supporting, conductive aerogel framework.[87] A hydrogel freeze-drying strategy was employed with pyrolysis to construct a macro-structure that intrinsically mimics the hierarchical porosity sought after in SAC design. During synthesis, dispersion and stabilization of single copper atoms were maintained by utilizing a phthalocyanine based copper complex, which is an established method by which Cu-based SACs are synthesized.[88] To enhance the dispersion of catalytic sites, while also providing a highly conductive support, a polypyrrole hydrogel was also combined with the sulfonated phthalocyanine copper complex, which served as a cross-linking agent for the hydrogel. This multiscale structural integration of coordinated single-atomic sites within a 3D framework successfully decoupled the active site density from the mass transport limitations that typically affect powder-coated electrodes.[89] The functional advantage of this 3D aerogel architecture was demonstrated in its unique dual-capability as both an electrocatalyst and a real-time sensor, capable of continuously monitoring local reactant and product concentrations, which is critical in an industrial setting with continuous production. While a manual doctor blade method was used for deposition of the hydrogel before pyrolysis, polypyrrole-based gels have been utilized with fabrication methods such as screen printing, DLP, and DIW.[90,91] The ability to dynamically regulate the catalytic process based on instantaneous feedback from the catalyst itself and the compatibility of hydrogels with various additive manufacturing methods demonstrates an ideal case for the usage of SACs in industrial applications, as the lab methods used to produce the catalyst coated electrode can be directly utilized in mass production.[92]

In the aforementioned cases, the primary advantages of utilizing additive manufacturing techniques were the scalability of the process and the ability to create complex geometries. However, the temperatures and timescales required for bulk pyrolysis may not be compatible with metal and/or support precursors such as MOFs, where aggregation of single atoms into clusters occurs due to decomposition or destabilization of the organic framework. To address these issues, methods that are capable of generating extreme temperatures over nanosecond timescales, such as rapid Joule heating or pulsed laser ablation, can be utilized.[93] In the case of pulsed laser ablation, for instance, a recent study demonstrated single atom loadings of 41.8 wt% in graphene quantum dots,[94] which is significantly higher than typical pyrolytic methods. Metal chloride precursors were first loaded onto various substrates through simply dispersion and drying, and the precursor was subsequently dispersed in hexane, after which a 1064 nm pulse laser with high fluence and frequency (5 J cm^{-3} and 35 kHz, respectively) was utilized to generate the SAC. Through dispersion in hexane, rapid quenching of the extreme temperatures generated after pulse application was achieved, while avoiding the solubilization or loss of the metal salts in the vapour plume. This was extended to create ''high entropy'' SACs, in which five elements (Pt, Ir, Cu, Co, and Ni) were simultaneously integrated into the support, which further extends the tunability of iridium SACs through both the support and additional metal dopants. While graphene quantum dots demonstrated a high single atom loading, it was found that implantation of single atoms was possible on inorganic substrates. Using the same method as previously mentioned, Pt single atoms were implanted on both metallic copper and TiO_2 nanoparticles as a support. This presents an extremely attractive alternative to using carbon-based supports, as carbon corrosion associated with high oxidative potentials used in industrial electrolysers may be completely bypassed.[95] Furthermore, implantation of single atoms may thus be possible directly on metal and metal oxide electrodes such as foils, foams, and plates, which are

Table 1 Comparison of synthetic techniques and resultant performance of the discussed Ir SACs

Catalyst	Method	Lattice or surface (L or S)	Electrolyte	OER overpotential @ 10 mA cm^{-2} (mV)	Tafel (mV dec^{-1})	Operational stability	Ref.
$Ir_{0.1}/Ni_9Fe$ SAC	*In situ* cryogenic photochemical reduction	S	1.0 M KOH	183	49	100 h at 1.43 V	55
Ir_{SA}–Ni_2P	Structural modification of iridium coated Ni nanospheres	S	1.0 M KOH	149	90.1	40 h at 1.5 V	56
Ir_1–PI@CP	Direct writing on polyimide support	S	0.5 M H_2SO_4	254	N/A	360 h at 10 mA cm^{-2}	60
$Ir_{0.06}Co_{2.94}O_4$	Templating of iridium single-atoms on cobalt spinel structures	L	0.1 M $HClO_4$	~294	45	200 h at 10 mA cm^{-2}	42
Ir_1Ru/TiO_2	Multi-step atomic assembly in ruthenium nanoclusters	L	0.5 M H_2SO_4	144	62.2	3200 at 10 mA cm^{-2}	64
Ir_{SA}–Ni_3N/Ni–Co–GO@CC	Electrochemical conversion of bulk metals into single-atoms	L	N/A	N/A	N/A	N/A	68

extensively utilized in industrial electrolysers simply due to their low cost and high durability.

Beyond the atomic scale, the efficiency of iridium SACs in practical water electrolysers is heavily dictated by the hydrodynamics of the OER, where bubble accumulation can block active sites and mechanically stress the delicate single-atom coordination environment.[96,97] As previously mentioned, additive manufacturing is uniquely suited to address this issue through the fabrication of ordered macro-architectures and flow geometries that are impossible to produce at industrially relevant scales *via* conventional manufacturing and coating methods. Aside from utilizing TPMS geometries in high flow electrochemical cells, conical arrays and hierarchically porous lattices are capable of inducing buoyancy-driven convection in static or low flow designs to rapidly detach oxygen bubbles.[98] Using water and gas transport vessels in trees as inspiration, which face similar gas and electrolyte transport issues, consumer grade DLP printers are now capable of creating biomimetic catalyst supports whose structures have evolved to address similar problems faced by gas evolving electrocatalysts.[99] For iridium SACs, this macroscopic active management is vital; by ensuring that the electrolyte is constantly refreshing the single-atom sites, local pH and concentration gradients are minimized, thereby reducing the likelihood of the iridium atoms leaching or aggregating under harsh local conditions.

The integration of SACs with 3D printing opens new avenues for reducing the time necessary to create industrial scale catalysts from lab-based techniques. Unlike traditional methods, where scaling up synthesis often alters the kinetics of nucleation and growth (leading to aggregation), 3D printing allows for the modular production of identical electrode units.[100] However, significant challenges remain. The rheological properties of inks must be carefully tuned to support high loadings of SAC precursors without compromising printability when utilizing DIW.[101] Furthermore, characterizing single atoms on complex, non-planar 3D surfaces presents a metrological challenge, as standard HAADF-STEM requires thin, electron-transparent samples. Non-destructive techniques such as X-ray Computed Tomography combined with X-ray Absorption Spectroscopy are thus essential to verify the uniformity of single-atom distribution throughout the printed monolith. Despite these hurdles, the convergence of single-atom catalysis and digital fabrication represents the logical next step in the evolution of iridium electrocatalysts, moving beyond the optimization of the active site to the optimization of the entire reactor environment. With the implementation of these synthetic technologies, iridium SACs sit on the cusp of widespread commercialization. Further refinement and development of these nascent techniques will result in iridium SACs playing a significant role in electrification worldwide based on the enhancement to water electrolysis alone, with further applications of these methods leading to breakthroughs throughout the field of catalysis.

Conclusions

The synthesis of iridium SACs has achieved remarkable milestones in minimizing noble metal loading and optimizing intrinsic activity, with the primary limitation being the complex synthesis unsuitable for scale-up, becoming a topic of increased interest. Synthesis of SACs is primarily hindered by the energetic tendency towards agglomeration of SACs, occurring in both superficial and lattice implemented single-atom structures. Many synthetic methods have been developed to overcome this limitation through various approaches, listed in Table 1, including the implementation of cryogenic freezing to halt redistribution, post synthetic modification of shelled nanoparticles and single-atom galvanic replacement. While the primary goal was to highlight current techniques used for the synthesis of iridium SACs, comparison of the exemplars of each of these techniques allows for a clearer understanding of the advantages and disadvantages of each. Superficial and lattice-implemented SACs both varied significantly without one clearly outperforming the other; however, it is notable that, of the acidic OER examples, the lattice implemented Ir_1Ru/TiO_2 reported the most impressive metrics. This is expected due to enhanced stability afforded by lattice implementation; however the low overpotential and high mass activity likely result from the beneficial relationship between Ir and Ru for the OER that has recently been demonstrated.[79] Of the more facile alkaline OER examples, Ir_{SA}–Ni_2P showed the lowest overpotential and highest mass activity, both of which are important for addressing the major industrial hurdles faced with commercial iridium electrolysis; however, additional stability testing is required. Despite these examples, as these techniques are further explored, it is likely that current limitations will be overcome and accurate comparison of trends will not be possible until a more comprehensive body of work emerges. The recent application of industrial scale-up of single-atom electrodes presents promising pathways to widespread production and commercialization, with the development of high stability polyimide printable complexes and scalable electrodeposition contributing to the development of the field. These advances allow implementation of the mechanistic advantages imparted by Ir SACs for the OER, including increased stable oxidation states, enhanced scaling and alternative mechanisms into existing water electrolysis systems.

Author contributions

Dylan Mcfarlane-Urbszat: concept, data curation, investigation, visualization, and writing – original draft, review and editing; Raoul Vaz: investigation, visualization, and writing – original draft, review and editing; Aicheng Chen: concept, supervision, funding acquisition, and writing – review and editing.

Conflicts of interest

There are no conflicts to declare.

Data availability

No primary research results, software or code have been included, and no new data were generated or analysed as part of this review.

Acknowledgements

This research was funded by the Discovery Grant from the Natural Sciences and Engineering Research Council of Canada (NSERC, RGPIN-2022-04238). A. C. acknowledges the NSERC and the Canada Foundation for Innovation (CFI) for the Canada Research Chair Award in Electrochemistry and Nanoscience.

References

1 T. C. Meisel, in *Encyclopedia of Geochemistry*, Springer, Cham, 2018, pp. 743–745.
2 C. Minke, M. Suermann, B. Bensmann and R. Hanke-Rauschenbach, *Int. J. Hydrogen Energy*, 2021, **46**, 23581–23590.
3 J. E. Ferrer and L. Victori, *Electrochimica Acta*, 1993, **38**, 1631–1636.
4 A. Aramata, T. Yamazaki, K. Kunimatsu and M. Enyo, *J. Phys. Chem.*, 1987, **91**, 2309–2314.
5 Q. Zhang, Z. Duan, Y. Wang, L. Li, B. Nan and J. Guan, *J. Mater. Chem. A*, 2020, **8**, 19665–19673.
6 A. Salverda, J. S. Dondapati, A. R. Thiruppathi and A. Chen, *J. Electrochem. Soc.*, 2020, **167**, 146506.
7 B. You, M. T. Tang, C. Tsai, F. Abild-Pedersen, X. Zheng and H. Li, *Adv. Mater.*, 2019, **31**, 1807001.
8 M. J. Craig, G. Coulter, E. Dolan, J. Soriano-López, E. Mates-Torres, W. Schmitt and M. García-Melchor, *Nat. Commun.*, 2019, **10**, 4993.
9 J. Fu, Y. Zhang, X. He, S. Zhang and Y. Ding, *Sep. Purif. Technol.*, 2026, **380**, 135429.
10 L. Moriau, M. Smiljanić, A. Lončar and N. Hodnik, *ChemCatChem*, 2022, **14**, e202200586.
11 C. Qiu, C. Sellers, Z.-Y. Wu, D. A. Cullen, E. Stavitski, A. Tayal, T.-U. Wi, M. Kodali, B. Erb, A. Smeltz, F.-Y. Chen, Y. Feng, Z. Yu, A. Elgazzar, T. Terlier, T. P. Senftle and H. Wang, *Nat. Nanotechnol.*, 2025, 1–9.
12 A. Chen, D. J. La Russa and B. Miller, *Langmuir*, 2004, **20**, 9695–9702.
13 L. Zhang, W. Li, S. Ren, Y. Zhang, W. Song, C. Wang and X. Lu, *Chem. Sci.*, 2025, **16**, 16081–16089.
14 H. Ou, D. Wang and Y. Li, *Nano Select*, 2021, **2**, 492–511.
15 X. Zhao, T. Mou, J. Long, A. Islam, S. Kang, N. N. Kariuki, D. J. Myers, P. Liu, J. A. Rodriguez, J. G. Chen and K. Sasaki, *J. Am. Chem. Soc.*, 2025, **147**, 43317–43329.
16 C. Wang and L. Feng, *Energy Adv.*, 2024, **3**, 14–29.
17 J. M. van der Zalm, J. Quintal, S. A. Hira, S. Chen and A. Chen, *Electrochim. Acta*, 2023, **439**, 141715.
18 C.-K. Hung, A. R. Thiruppathi, N. Burns, C. McGuire, J. Quintal, D.-T. Jiang, S. Kycia and A. Chen, *ACS Catal.*, 2024, **14**, 5416–5428.
19 K. Zhang, X. Liang, Y. Wang, Y. Zou, X. Zhao, H. Chen and X. Zou, *Nat. Commun.*, 2025, **16**, 8164.
20 F. B. Holde, P. Sebastián-Pascual, K. N. Dalby, E. Gómez and M. Escudero-Escribano, *Electrochim. Acta*, 2023, **467**, 143058.
21 B. Qiao, A. Wang, X. Yang, L. F. Allard, Z. Jiang, Y. Cui, J. Liu, J. Li and T. Zhang, *Nat. Chem.*, 2011, **3**, 634–641.
22 J. Quintal, C. McGuire, T. Shi, W.-H. Huang, D. Chow, C.-K. Hung, D.-T. Jiang, B. J. Hwang and A. Chen, *J. Phys. Chem. Lett.*, 2024, **15**, 9208–9215.
23 H. Q. Pham, H. T. Q. Pham, Q. Huynh and T. T. Huynh, *Coord. Chem. Rev.*, 2023, **486**, 215143.
24 X. Lu, Z. Wang, B. Yuan, L. Zhu, M. Shen, D. Du, Y. Zhou, W. Zhu and Y. Lin, *ACS Energy Lett.*, 2025, **10**, 3763–3774.
25 Z. Chen, A. G. Walsh and P. Zhang, *Acc. Chem. Res.*, 2024, **57**, 521–532.
26 G. Su, J. Yang and J. Yin, *ChemElectroChem*, 2025, **12**, e202400559.
27 B. B. Sarma, F. Maurer, D. E. Doronkin and J.-D. Grunwaldt, *Chem. Rev.*, 2022, **123**, 379–444.
28 X. Shao, X. Yang, J. Xu, S. Liu, S. Miao, X. Liu, X. Su, H. Duan, Y. Huang and T. Zhang, *Chem*, 2019, **5**, 693–705.
29 N. K. Zimmerli, C. R. Müller and P. M. Abdala, *Trends Chem.*, 2022, **4**, 807–821.
30 M. W. Terban and S. J. L. Billinge, *Chem. Rev.*, 2022, **122**, 1208–1272.
31 I. Kappel, M. W. Terban, M. Vennewald, N. M. Sackers, A. Iemhoff, J. C. Baums, S. Leiting, M. Etter, P. J. C. Hausoul, R. Palkovits and C. Weidenthaler, *Mater. Today Chem.*, 2025, **47**, 102776.
32 C. E. White, J. L. Provis, T. Proffen, D. P. Riley and J. S. J. van Deventer, *Phys. Chem. Chem. Phys.*, 2010, **12**, 3239–3245.
33 H. Sun, Q. Liu, Z. Gao, L. Geng, Y. Li, F. Zhang, J. Yan, Y. Gao, K. Suenaga, L. Zhang, Y. Tang and J. Huang, *J. Mater. Chem. A*, 2022, **10**, 6096–6106.
34 M. J. Zachman, A. Serov, X. Lyu, S. McKinney, H. Yu, M. P. Oxley, L. Spillane, E. F. Holby and D. A. Cullen, *Electrochim. Acta*, 2023, **469**, 143205.
35 S. E. Jun, Y.-H. Kim, J. Kim, W. S. Cheon, S. Choi, J. Yang, H. Park, H. Lee, S. H. Park, K. C. Kwon, J. Moon, S.-H. Kim and H. W. Jang, *Nat. Commun.*, 2023, **14**, 609.
36 A. M. Blackburn, C. Cordoba, M. R. Fitzpatrick and R. A. McLeod, *Nat. Commun.*, 2025, **16**, 8977.
37 S. Iijima, I. Ohnishi and Z. Liu, *Sci. Rep.*, 2021, **11**, 18022.
38 R. Chatterjee, C. Weninger, A. Loukianov, S. Gul, F. D. Fuller, M. H. Cheah, T. Fransson, C. C. Pham, S. Nelson, S. Song, A. Britz, J. Messinger, U. Bergmann, R. Alonso-Mori, V. K. Yachandra, J. Kern and J. Yano, *J. Synchrotron Radiat.*, 2019, **26**, 1716–1724.
39 A. Uzun, V. Ortalan, N. D. Browning and B. C. Gates, *Chem. Commun.*, 2009, 4657–4659.
40 X. Yu, Z. Rao, G. Chen, Y. Yang, S. Yoon, L. Liu, Z. Huang, M. Widenmeyer, H. Guo, G. Homm, U. Kunz, X. Liu, E. Ionescu, L. Molina-Luna, X. Tu, Y. Zhou and A. Weidenkaff, *Angew. Chem., Int. Ed.*, 2024, **63**, e202404196.

41 A. Kumar, M. Gil-Sepulcre, J. Lee, V. Q. Bui, Y. Wang, O. Rüdiger, M. G. Kim, S. DeBeer and H. Tüysüz, *Adv. Mater.*, 2024, **36**, 2401648.
42 J. Shan, C. Ye, S. Chen, T. Sun, Y. Jiao, L. Liu, C. Zhu, L. Song, Y. Han, M. Jaroniec, Y. Zhu, Y. Zheng and S.-Z. Qiao, *J. Am. Chem. Soc.*, 2021, **143**, 5201–5211.
43 D. Roy and K. Deori, *Nanoscale Adv.*, 2025, **7**, 1243–1271.
44 B. Yang, M. Li, Z. Zhang, S. Chen, M. Wang, L. Sheng, L. Deng, R. Si, M. Fan and H. Chen, *Appl. Catal., B*, 2024, **340**, 123227.
45 R. Li, G. Yang, L. Zhao, X. Tan, R. Yuan and S. Chen, *Anal. Chem.*, 2025, **97**, 20127–20136.
46 Y. Pan, X. Wang, W. Zhang, L. Tang, Z. Mu, C. Liu, B. Tian, M. Fei, Y. Sun, H. Su, L. Gao, P. Wang, X. Duan, J. Ma and M. Ding, *Nat. Commun.*, 2022, **13**, 3063.
47 Z. Wei, Y. Ding, W. Shi, F. Zhang, Y. Song, X. Cui, Y. Guo, L. Sun, Q. Jiang and B. Zhang, *Nat. Commun.*, 2025, **16**, 8145.
48 J. Luo, G. I. N. Waterhouse, L. Peng and Q. Chen, *Ind. Chem. Mater.*, 2023, **1**, 486–500.
49 W. Li, Z. Guo, J. Yang, Y. Li, X. Sun, H. He, S. Li and J. Zhang, *Electrochem. Energy Rev.*, 2022, **5**, 9.
50 W. Tan, S. Xie, Y. Cai, H. Yu, K. Ye, M. Wang, W. Diao, L. Ma, S. N. Ehrlich, F. Gao, L. Dong and F. Liu, *Environ. Sci. Technol.*, 2023, **57**, 12501–12512.
51 S. Li, W. Wang, H. Wu, X. Wang, S. Ding, J. Liu, X. Zhang, J. Sun, C. Fu and M. Zhou, *Nat. Commun.*, 2025, **16**, 8796.
52 W. Ko, J. Shim, H. Ahn, H. J. Kwon, K. Lee, Y. Jung, W. H. Antink, C. W. Lee, S. Heo, S. Lee, J. Jang, J. Kim, H. S. Lee, S.-P. Cho, B.-H. Lee, M. Kim, Y.-E. Sung and T. Hyeon, *J. Am. Chem. Soc.*, 2025, **147**, 2369–2379.
53 X. Zheng, J. Tang, A. Gallo, J. A. Garrido Torres, X. Yu, C. J. Athanitis, E. M. Been, P. Ercius, H. Mao, S. C. Fakra, C. Song, R. C. Davis, J. A. Reimer, J. Vinson, M. Bajdich and Y. Cui, *Proc. Natl. Acad. Sci. U. S. A.*, 2021, **118**, e2101817118.
54 S. Guo, Y. Zhao, C. Wang, H. Jiang and G. J. Cheng, *ACS Appl. Mater. Interfaces*, 2020, **12**, 26068–26075.
55 K. Gilmore, J. Vinson, E. L. Shirley, D. Prendergast, C. D. Pemmaraju, J. J. Kas, F. D. Vila and J. J. Rehr, *Comput. Phys. Commun.*, 2015, **197**, 109–117.
56 Q. Wang, Z. Zhang, C. Cai, M. Wang, Z. L. Zhao, M. Li, X. Huang, S. Han, H. Zhou, Z. Feng, L. Li, J. Li, H. Xu, J. S. Francisco and M. Gu, *J. Am. Chem. Soc.*, 2021, **143**, 13605–13615.
57 R. Nakamura, J.-G. Lee, H. Mori and H. Nakajima, *Philos. Mag.*, 2008, **88**, 257–264.
58 A. Kaliyaraj Selva Kumar, Y. Zhang, D. Li and R. G. Compton, *Electrochem. Commun.*, 2020, **121**, 106867.
59 F. Xie, X. Cui, X. Zhi, D. Yao, B. Johannessen, T. Lin, J. Tang, T. B. F. Woodfield, L. Gu and S.-Z. Qiao, *Nat. Synth.*, 2023, **2**, 129–139.
60 L. Zhang, J. Bai, S. Zhang, Y. Liu, J. Ye, W. Fan, E. Debroye and T. Liu, *ACS Nano*, 2024, **18**, 22095–22103.
61 S. Park, S. Ban, N. Zavanelli, A. E. Bunn, S. Kwon, H. Lim, W.-H. Yeo and J.-H. Kim, *ACS Appl. Mater. Interfaces*, 2023, **15**, 2092–2103.
62 M. Bogar, Y. Yakovlev, S. Pollastri, R. Biagi, H. Amenitsch, R. Taccani and I. Matolínová, *J. Power Sources*, 2024, **615**, 235070.
63 C. Pu, F. Liu, H. Xu, G. Chen, G. Tian, S. Qi and D. Wu, *Mater. Today Chem.*, 2023, **33**, 101679.
64 S. Li, L. Deng, S.-F. Hung, S. Zhao, L. Wang, Y. Hao, Y. Long, B. Li, Y.-H. Hsu, Y.-Y. Chen, Y. Zhang, T.-Y. Chen, F. Hu, L. Li, Y. Hu, Y. Wu and S. Peng, *Adv. Mater.*, 2025, **38**(3), e07340.
65 *Technical Targets for Proton Exchange Membrane Electrolysis*, https://www.energy.gov/eere/fuelcells/technical-targets-proton-exchange-membrane-electrolysis, (accessed December 22, 2025).
66 S. La Niece and P. Craddock, *Metal Plating and Patination*, Butterworth-Heinemann, 1993, pp. 284–290.
67 N. Sabouhanian, B. J. R. Laframboise, J. Quintal, Z. Su, L. D. Chen, J. Lipkowski and A. Chen, *Electrochim. Acta*, 2026, **550**, 148126.
68 S. Wang, M. Lu, X. Xia, F. Wang, X. Xiong, K. Ding, Z. Pang, G. Li, Q. Xu, H.-Y. Hsu, S. Hu, L. Ji, Y. Zhao, J. Wang, X. Zou and X. Lu, *Proc. Natl. Acad. Sci. U. S. A.*, 2024, **121**, e2319136121.
69 Z. Zhang, H. Zhao, S. Xi, X. Zhao, X. Chi, H. Bin Yang, Z. Chen, X. Yu, Y.-G. Wang, B. Liu and P. Chen, *Nat. Commun.*, 2025, **16**, 1301.
70 A. F. Pedersen, M. Escudero-Escribano, B. Sebok, A. Bodin, E. Paoli, R. Frydendal, D. Friebel, I. E. L. Stephens, J. Rossmeisl, I. Chorkendorff and A. Nilsson, *J. Phys. Chem. B*, 2018, **122**, 878–887.
71 X. Han, T. Mou, S. Kang, A. Islam, X. Zhao, K. Sasaki, J. A. Rodriguez, Q. Chang, P. Liu and J. G. Chen, *Angew. Chem., Int. Ed.*, 2025, **64**, e202507468.
72 M. Retuerto, L. Pascual, O. Piqué, P. Kayser, M. A. Salam, M. Mokhtar, J. A. Alonso, M. Peña, F. Calle-Vallejo and S. Rojas, *J. Mater. Chem. A*, 2021, **9**, 2980–2990.
73 J. Zhang, Y. Zhao, C. Chen, Y.-C. Huang, C.-L. Dong, C.-J. Chen, R.-S. Liu, C. Wang, K. Yan, Y. Li and G. Wang, *J. Am. Chem. Soc.*, 2019, **141**, 20118–20126.
74 L. Bahri, F. T. Dajan, M. G. Sendeku and K. Harrath, *Adv. Theory Simul.*, 2025, **8**, 2500045.
75 W. Zhang, Q. Fu, Q. Luo, L. Sheng and J. Yang, *JACS Au*, 2021, **1**, 2130–2145.
76 A. Grimaud, O. Diaz-Morales, B. Han, W. T. Hong, Y.-L. Lee, L. Giordano, K. A. Stoerzinger, M. T. M. Koper and Y. Shao-Horn, *Nat. Chem.*, 2017, **9**, 457–465.
77 W. Li, J. Zhang, C. Yang, Z. Geng, X. Chen, Q. Liu, B. Wang and L. Wang, *J. Am. Chem. Soc.*, 2025, **147**, 40697–40707.
78 Z. Duan, Z. Cui, Z. Gao, W. Xu, Y. Liang, H. Jiang, Z. Li, F. Wang and S. Zhu, *ACS Catal.*, 2025, **15**, 16882–16892.
79 W. Zhu, X. Song, F. Liao, H. Huang, Q. Shao, K. Feng, Y. Zhou, M. Ma, J. Wu, H. Yang, H. Yang, M. Wang, J. Shi, J. Zhong, T. Cheng, M. Shao, Y. Liu and Z. Kang, *Nat. Commun.*, 2023, **14**, 5365.
80 P. Jovanovič, N. Hodnik, F. Ruiz-Zepeda, I. Arčon, B. Jozinović, M. Zorko, M. Bele, M. Šala, V. S. Šelih, S. Hočevar and M. Gaberšček, *J. Am. Chem. Soc.*, 2017, **139**, 12837–12846.
81 C. Jia, Q. Sun, R. Liu, G. Mao, T. Maschmeyer, J. J. Gooding, T. Zhang, L. Dai and C. Zhao, *Adv. Mater.*, 2024, **36**, 2404659.
82 S. A. Lee, S. Eon Jun, S. Hwa Park, K. Chang Kwon, J. Hun Kang, M. Sang Kwon and H. Won Jang, *EES Catal.*, 2024, **2**, 49–70.
83 Y. Zhang, X. Li and A. Klinkova, *Int. J. Hydrogen Energy*, 2021, **46**, 11071–11083.
84 J. Luo, V. Ruta, I. S. Kwon, J. Albertazzi, N. Allasia, O. Nevskyi, V. Busini, D. Moscatelli and G. Vilé, *Adv. Funct. Mater.*, 2024, **34**, 2404794.
85 M. S. Islam, F. T. Zohra and B. Asiabanpour, *Int. J. Adv. Manuf. Technol.*, 2025, **140**, 2813–2832.
86 F. Rocha, R. Delmelle, C. Georgiadis and J. Proost, *Adv. Energy Mater.*, 2023, **13**, 2203087.
87 P. Li, L. Liao, Z. Fang, G. Su, Z. Jin and G. Yu, *Proc. Natl. Acad. Sci. U. S. A.*, 2023, **120**, e2305489120.
88 L. Cui, L. Cui, Z. Li, J. Zhang, H. Wang, S. Lu and Y. Xiang, *J. Mater. Chem. A*, 2019, **7**, 16690–16695.
89 J. Lopata, Z. Kang, J. Young, G. Bender, J. W. Weidner and S. Shimpalee, *J. Electrochem. Soc.*, 2020, **167**, 064507.
90 C. Song, Q. Zhao, T. Xie and J. Wu, *J. Mater. Chem. A*, 2024, **12**, 5348–5356.
91 M. Ho, A. B. Ramirez, N. Akbarnia, E. Croiset, E. Prince, G. G. Fuller and M. Kamkar, *Adv. Funct. Mater.*, 2025, **35**, 2415507.
92 G. A. Price, D. Mallik and M. G. Organ, *J. Flow Chem.*, 2017, **7**, 82–86.
93 Y. Sha, F. Moissinac, M. Zhu, K. Huang, H. Guo, L. Wang, Y. Liu, L. Li, A. Thomas and Z. Liu, *ACS Appl. Mater. Interfaces*, 2023, **15**, 51004–51012.
94 B. Wang, X. Zhu, X. Pei, W. Liu, Y. Leng, X. Yu, C. Wang, L. Hu, Q. Su, C. Wu, Y. Yao, Z. Lin and Z. Zou, *J. Am. Chem. Soc.*, 2023, **145**, 13788–13795.
95 S. Möller, S. Barwe, J. Masa, D. Wintrich, S. Seisel, H. Baltruschat and W. Schuhmann, *Angew. Chem., Int. Ed.*, 2020, **59**, 1585–1589.
96 J. Park, M. J. Kim, Y. Kim, S. Lee, S. Park and W. Yang, *ACS Energy Lett.*, 2025, **10**, 212–237.
97 Z. Chen, J. Liu and K. P. Loh, *Acc. Mater. Res.*, 2023, **4**, 27–41.
98 Y. Xun, K. Zhang, W. Jonhson and J. Ding, *APL Mater.*, 2023, **11**, 061119.
99 T. Zeng, B. Guo, Z. Xu, F. Mo, X. Chen, L. Wang, Y. Ding and J. Bai, *Adv. Sci.*, 2023, **10**, 2207495.
100 S. Mitchell, N.-L. Michels and J. Pérez-Ramírez, *Chem. Soc. Rev.*, 2013, **42**, 6094–6112.
101 D. Yang, Y. Guo, H. Tang, D. Yang, P. Ming, C. Zhang, B. Li and S. Zhu, *Int. J. Hydrogen Energy*, 2022, **47**, 8956–8964.